IEEE ComSoc IEEE Open Journal of the Communications Society

Received XX Month, XXXX; revised XX Month, XXXX; accepted XX Month, XXXX; Date of publication XX Month, XXXX; date of current version 22 December, 2025.

Dual Satellite STBC Combining Under Imperfect Symbol Time Alignment

CARLOS L. MARCOS ROJAS,[1] *Graduate Student Member, IEEE*, JORGE L. GONZALEZ RIOS,[1] *Member, IEEE*, LUIS M. GARCES SOCARRAS,[1] *Member, IEEE*, VIBHUM SINGH,[1] *Member, IEEE*, RAUDEL CUIMAN MARQUEZ,[1] *Member, IEEE*, JUAN C. MERLANO DUNCAN, [1] *Senior Member, IEEE*, Vu Nguyen HA,[1] *Senior Member, IEEE*, SYMEON CHATZINOTAS,[1] *Fellow, IEEE*, and BJÖRN OTTERSTEN,[1] *Fellow , IEEE*

[1]Interdisciplinary Centre for Security, Reliability and Trust (SnT), University of Luxembourg, Luxembourg

CORRESPONDING AUTHOR: CARLOS L. MARCOS ROJAS (e-mail: carlos.marcosrojas@uni.lu).

This work was supported by the Luxembourg National Research Fund (FNR), through the CORE Project (ARMMONY): Ground-based distributed beamforming harmonization for the integration of satellite and Terrestrial networks, under Grant FNR16352790.

ABSTRACT In distributed satellite communication systems, spatial diversity techniques such as Space-Time Block Coding (STBC) offer an attractive opportunity to enhance the link's capabilities without additional spectrum consumption. One of the major challenges that still remains is the degradation of the Signal-to-Interference-plus-Noise Ratio (SINR) at the receiver, primarily due to time misalignment between satellites. This paper presents a robust receiver architecture that demonstrates strong resilience against SINR degradation caused by time misalignment between satellites and maintains robust performance even under additional impairments such as power imbalance and Doppler shifts. Moreover, we present an efficient implementation of the receiver, which combines both software and hardware platforms.

INDEX TERMS STBC, Spatial Diversity, Satellite Communications, SINR, Time Misalignment.

I. INTRODUCTION

NOn-geostationary orbit (NGSO) satellite constellations are expanding rapidly, with the potential to transform global communications by enabling ubiquitous coverage and significantly boosting satellite network capacity [1]. One promising approach to fully exploit the capabilities of these constellations is the simultaneous use of signals from multiple satellites, which can substantially improve both spectral efficiency and link reliability for broadcast and related services [2]. Within this context of multi-satellite systems, Space-Time Block Coding (STBC) emerges as a compelling, albeit innovative, candidate technique. If effectively adapted, STBC could offer considerable advantages, such as increased received Signal-to-Noise Ratio (SNR), theoretically up to 3 dB from combining two signals of the same power [3], and enhanced resilience against channel blockages and time-varying fading encountered in mobile satellite environments [4]. Compared to other cooperative schemes, STBC is more resilient to fast differential phase variations, particularly those induced by Doppler shifts and payload phase noise [4]. As such, its application could provide an interesting alternative for improving handover procedures in highly dynamic NGSO settings. Unlike network coding, which operates at higher layers and depends on successful packet transmissions, STBC inherently provides symbol-level transmit diversity, significantly improving signal robustness and SNR [5]. Furthermore, its low computational complexity, predictable performance gains, and limited reliance on Channel State Information (CSI) make STBC well-suited for latency-sensitive and resource-constrained wireless applications, offering a more direct and deterministic solution compared to network coding [6], [7].

Despite its advantages, the practical implementation of STBC in distributed multi-satellite NGSO architectures is highly challenging, primarily due to the stringent time alignment requirements between the signals. In conventional systems with co-located transmit antennas sharing a common oscillator, time-aligned reception is inherently achievable. However, in distributed satellite systems, this assumption becomes problematic. While prior research has focused on improving metrics such as spectral efficiency [8], physical layer security [9], and channel capacity [10], the assumption of synchronous waveform arrival at

This work is licensed under a Creative Commons Attribution 4.0 License. For more information, see https://creativecommons.org/licenses/by/4.0/

the user terminal (UT) remains prevalent [11]. In practice, achieving precise time alignment from geographically displaced satellites is exceedingly difficult [12], [13]. Even with stringent synchronization loops established between the transmitting satellites themselves, the inherent uncertainty in the precise position of the intended receiver, compounded by differing and dynamically varying propagation delays, means that the received waveforms will inevitably exhibit relative time offsets [14].

Issues concerning the performance of STBC systems under imperfect symbol time synchronization have been explored in prior studies, including [15], [16], and [17]. These works primarily address synchronization errors resulting from oscillator mismatches between the transmitter and receiver. However, they do not consider differential symbol time misalignment caused by varying propagation delays in distributed relay networks. Other contributions, such as [18], investigate time misalignment among relayed signals and propose a detection scheme based on Parallel Interference Cancellation (PIC) to mitigate the resulting degradation in STBC performance. In [19], the authors introduce a near-optimum Maximum Likelihood (ML) detection algorithm that surpasses conventional STBC detection methods when differential symbol time misalignment reaches up to 0.5 symbol periods. Additionally, [20] presents a zero-padded time-reversal quasi-orthogonal STBC scheme, combined with an ML detector, to address the misalignment between the symbols.

Addressing these challenges, our prior work in [21] proposed a novel approach for symbol time synchronization and tracking at the UT for the signal coming from two satellites. The method leverages a feedback channel to compensate for substantial integer-symbol time misalignments and to estimate the remaining fractional offset at the UT. Furthermore, [22] presented a diversity combining scheme capable of supporting STBC transmissions in the presence of time misalignment between signals from multiple NGSO satellites. This technique relies on an extended Inter-Symbol Interference (ISI) cancellation or compensation mechanism operating on blocks of finite size. Although effective in theory, the approach requires the computation of a compensation matrix for a block of N symbols, involving the inversion of a $2N \times 2N$ matrix. The subsequent decoding involves a matrix-by-vector multiplication. The computational burden associated with these operations, particularly the large matrix inversion, can render the decoder implementation impractical for real-time, resource-constrained UTs.

Motivated by the preceding discussion, this paper proposes the following contributions:

- A UT architecture featuring a dual digital reception chain, enabling simultaneous synchronization with two satellites and the combination of STBC-encoded symbols under conditions of imperfect time alignment.
- A novel low-complexity receiver architecture that exploits the block circulant properties of the solution matrices introduced in [22] used to compensate for the time misalignment between the STBC encoded signals. The proposed approach leverages eigen-block decomposition based on Fourier analysis, significantly reducing the required computational resources compared to conventional direct inversion techniques [23]–[25].
- A real-time capable hardware demonstrator for combining dual symbol streams, which exploits the block circulant structure of the solution matrix. The resulting compensation matrix is represented as a set of "stripes", (vertically appended rows or vectors of blocks) that correspond directly to the coefficients of a bank of Finite Impulse Response (FIR) filters. These filters are applied to the incoming signal symbols at the receiver, enabling efficient and structured symbol combination.

Building on this structure, the coefficients corresponding to each FIR filter stripe are computed using channel estimates acquired at the receiver. These coefficients are periodically updated to reflect changes in the communication channel, ensuring that the symbol combination remains both adaptive and robust under dynamic conditions. We assess the application of this method to single-carrier communications, with a particular focus on its adaptation to standard physical layer protocols such as DVB-S2X, considering its periodical pilot structure and physical layer scrambling. The efficacy of the proposed scheme is evaluated through analytical derivations of expected performance gains under various Medium Earth Orbit (MEO) satellite channel conditions. These theoretical results are further validated by extensive computer simulations and experimental assessments in a laboratory environment using Software Defined Radio (SDR) platforms, where transmitter, receiver, and channel emulation functionalities are implemented on Field Programmable Gate Arrays (FPGAs). Although the methods proposed in this work can theoretically be extended to configurations involving more than two satellites, as demonstrated in [22], large NGSO satellite constellations typically avoid frequency reuse over the same coverage area to mitigate interference. Nevertheless, the proposed approach remains applicable when two satellites reuse the spectrum within a localized spot beam, without requiring frequency reuse across all satellites within the terminal's field of view. In this sense, STBC is not proposed as an efficient method for combining the power of more than two satellites, but rather as a means of providing link resiliency and continuous coverage.

The remainder of this paper is organized as follows. Section II provides the system model and describes the operational scenario. Section III details the proposed efficient STBC processing scheme and algorithms. Section IV describes the experimental setup, and Section V presents

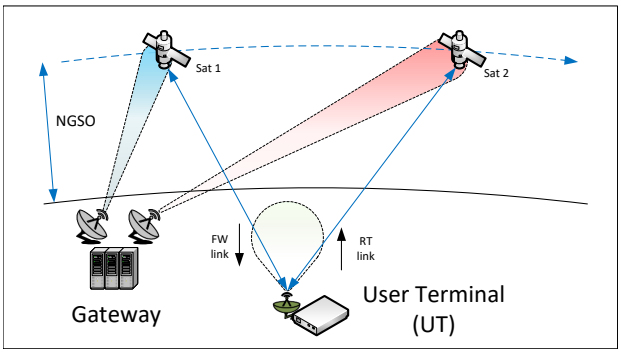

Fig. 1. Dual satellite STBC communication scenario, with a forward link and a return link.

the simulations and experimental results. Finally, Section VI concludes the paper, summarizing key contributions and suggesting directions for future research.

Notations: **Bold** lowercase and uppercase letters represent vectors and matrices, respectively; superscripts $(\cdot)^*$, $(\cdot)^T$ and $(\cdot)^H$ denote the conjugate, transpose and conjugate transpose operators, respectively. $\|\cdot\|_F^2$ represent the Frobenius norm squared of a matrix and $\otimes$ denotes the Kronecker product; $\circledast$ denotes circular convolution and $*$ represents linear convolution. The real and imaginary parts of a complex scalar symbol are represented by s_R and s_I, respectively.

II. SYSTEM DESCRIPTION

Consider the system model represented in Fig. 1, where a UT with a single wide-beam antenna can receive signals from two distinct NGSO satellites [26]. To provide spatial diversity, the same information is transmitted by the two satellites according to the STBC technology. The two superimposed waveforms incorporate orthogonal pilot sequences, enabling independent synchronization for each satellite. Although the UT employs a single radio frequency (RF) input, it requires two separate digital reception chains (one per satellite) as well as a diversity processing block, as illustrated in Fig. 2.

The encoded data symbols are embedded within the DVB-S2X waveform standard, where each waveform is transmitted using a distinct Walsh-Hadamard sequence to enable independent synchronization chains. Despite this separation, both waveforms occupy the same frequency spectrum. As a result, while each synchronization chain can lock onto only one of the two signals, both waveforms are in superposition within each chain.

Due to the relative motion between the satellites and the UT, each signal experiences a distinct and time-varying propagation path, resulting in misalignment between the incoming symbols. This misalignment not only degrades the performance of STBC due to inter-symbol delays, but also introduces ISI caused by improper time synchronization at the input of the Square Root Raised Cosine (SRRC) filter. Moreover, even after compensating for the integer symbol time misalignment as proposed

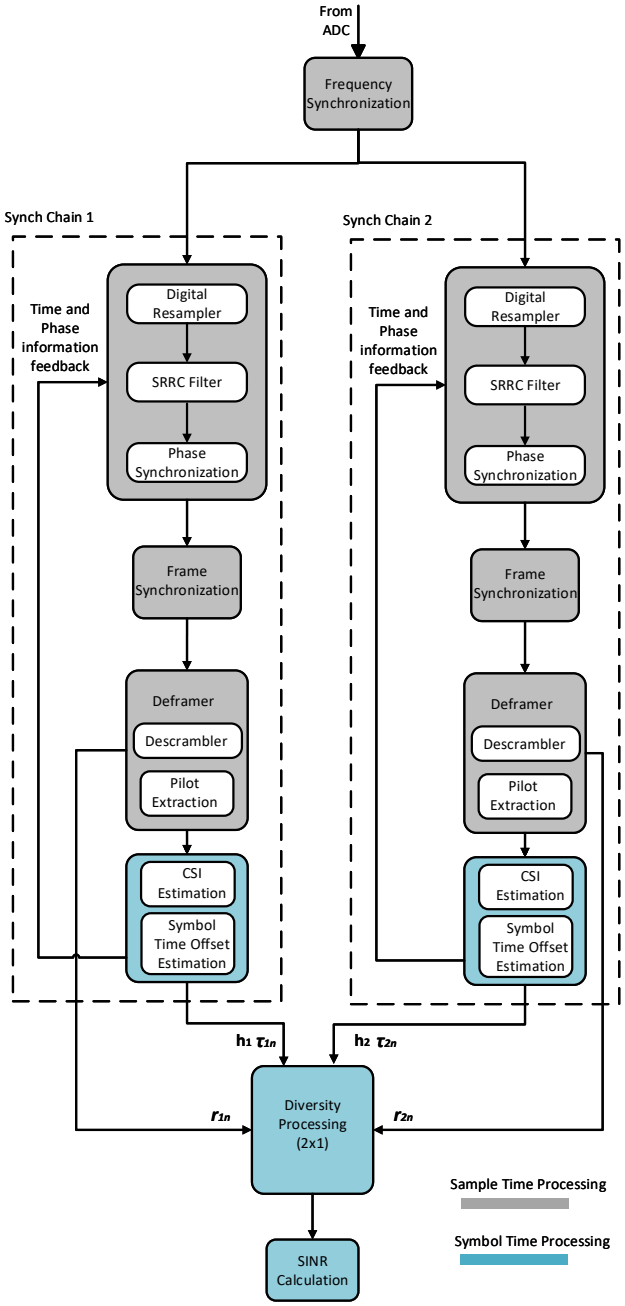

Fig. 2. Receiver schematic with two synchronization chains (one for each satellite signal) and a diversity processing block that combines such signals after synchronization.

in [21], the remaining fractional misalignment exhibits a time-varying behavior that must be continuously estimated.

Once the Automatic Gain Control (AGC) and synchronization chains in Fig. 2 have locked onto their respective signals, the received symbols r_{1n} and r_{2n}, observed at the output of each chain, can be mathematically modeled as in (1) and (2). Let the synchronized encoded symbols from the first and second chains be denoted by a_n and b_n, respectively. It is important to note that each

synchronization chain also includes the inverse sequence of encoded symbols, which remains unsynchronized and therefore acts as a source of interference in the received signal.

$$r_{1n} = a_n + \alpha_n e^{j\theta_n}\left(\sum_{k=-\infty}^{\infty} b_k g(nTs - kTs - \tau_n)\right) + z_n, \quad (1)$$

$$r_{2n} = b_n + \frac{1}{\alpha_n} e^{-j\theta_n}\left(\sum_{k=-\infty}^{\infty} a_k g(nTs - kTs + \tau_n)\right) + z_n. \quad (2)$$

Herein, α_n, θ_n, and $\tau_n = \tau_{1n} - \tau_{2n}$ denote the differential amplitude, phase, and symbol time, between the incoming signals, where τ_{1n} and τ_{2n} are the symbol time misalignment of the individual signals before the compensation applied by the digital resampler. The function g represents the impulse response of the overall channel, encompassing the transmitter filter, the wireless channel, and the receiver filter, under the assumption of a single-path (non-dispersive) scenario. Ts denote the symbol period, and z_n corresponds to additive white Gaussian noise (AWGN) filtered by the SRRC filter. To combine the signals, a diversity processing block is introduced after both synchronization chains. This block utilizes the received symbols, Alamouti dispersion matrices, CSI estimation, and symbol time misalignment estimation to recover the original transmitted information.

III. DIVERSITY PROCESSING 2x1

The overall communication system illustrated in Fig. 1 can be characterized as a Multiple-Input Single-Output (MISO) configuration, in which each signal transmitted by the gateway (GW) is independently amplified and forwarded by a separate satellite. Spatial diversity is achieved by transmitting identical information (with different STBC codes) through both satellites, resulting in two statistically independent propagation channels. In the proposed scenario, we assume a relatively directive antenna operating with a signal bandwidth that is significantly smaller than the channel's coherence bandwidth. Under these conditions, the multipath delay spread is negligible due to the dominant line-of-sight component and minimal scattering, allowing the channel to be modeled as flat fading. This channel is represented by a complex coefficient h, which varies over time as a result of factors such as atmospheric conditions, satellite motion, and user terminal (UT) mobility.

A. Signal model of STBC

In a transmit diversity system with N_T antennas, a generic STBC codeword is sent over an interval of P symbol periods. Assuming that the channel propagation conditions remain invariant over the length of P, the transmitted codeword can be written as a matrix $\mathbf{S}$ with dimensions $P \times N_T$ that contains K complex symbols. Hence, the code length is P and its code rate (transmitted symbols per codeword) $R = \frac{K}{P}$ [27]. Then $\mathbf{S}$ can be expressed as:

$$\mathbf{S} = \sum_{i=1}^{K} (\mathbf{A}_i^R s_i^R + \mathbf{A}_i^I s_i^I) \quad (3)$$

where the information symbols are $s_i = s_i^R + s_i^I$ and s_i^R and s_i^I are the real (I) and imaginary (Q) components of s_i. Matrices $\mathbf{A}_i^R$ and $\mathbf{A}_i^I$, both of dimension $P \times N_T$, are called the encoding matrices of the STBC.

In the case of Alamouti STBC [3], with $N_T = K = P = 2$, the codeword matrix containing the encoded symbols can be written as:

$$\mathbf{S} = \begin{bmatrix} s_1 & s_2 \\ -s_2^* & s_1^* \end{bmatrix}, \quad (4)$$

where the corresponding encoding matrices are:

$$\mathbf{A}_1^R = \begin{bmatrix} 1 & 0 \\ 0 & 1 \end{bmatrix}, \mathbf{A}_2^R = \begin{bmatrix} 0 & 1 \\ -1 & 0 \end{bmatrix}, \mathbf{A}_1^I = \begin{bmatrix} 1 & 0 \\ 0 & -1 \end{bmatrix}, \mathbf{A}_2^R = \begin{bmatrix} 0 & 1 \\ 1 & 0 \end{bmatrix}. \quad (5)$$

The row of the STBC codeword represents the symbol to be transmitted at a particular time slot, while the column represents the symbol to be transmitted at a specific transmit antenna. Each encoding branch represents an independent communication link with a code rate of 1, which translates to an increase in the spectral efficiency when the two branches are received with the same power.

The encoded symbols are then modified by the channel coefficients $h_1 = \alpha_n e^{j\theta_n}$ and $h_2 = \alpha_n h_1 e^{j\theta_n}$ respectively, and subsequently impacted by the differential time of arrival at the UT. Since the Alamouti scheme encodes two symbols over two consecutive time slots, a common representation of the received signal involves organizing the symbols into a column vector, stacking their real and imaginary components as

$$\mathbf{s} = \begin{bmatrix} s_{1R} \\ s_{1I} \\ s_{2R} \\ s_{2I} \end{bmatrix}. \quad (6)$$

Each symbol stream in the corresponding transmitter is encoded using the stack representation of the encoding matrices in (5)

$$\mathbf{A}_1 = \begin{bmatrix} 1 & 0 & 0 & 0 \\ 0 & 1 & 0 & 0 \\ 0 & 0 & -1 & 0 \\ 0 & 0 & 0 & 1 \end{bmatrix}, \quad (7a)$$

$$\mathbf{A}_2 = \begin{bmatrix} 0 & 0 & 1 & 0 \\ 0 & 0 & 0 & 1 \\ 1 & 0 & 0 & 0 \\ 0 & -1 & 0 & 0 \end{bmatrix}. \quad (7b)$$

Then at the receiver, the differential flat fading channel effects can be written in a stack representation as well, given by the matrix as

$$\mathbf{H}_i = \begin{bmatrix} \Re(h_i) & \Im(h_i) & 0 & 0 \\ -\Im(h_i) & \Re(h_i) & 0 & 0 \\ 0 & 0 & \Re(h_i) & \Im(h_i) \\ 0 & 0 & -\Im(h_i) & \Re(h_i) \end{bmatrix}, i \in \{1,2\}. \quad (8)$$

This article has been accepted for publication in IEEE Open Journal of the Communications Society. This is the author's version which has not been fully edited and content may change prior to final publication. Citation information: DOI 10.1109/OJCOMS.2025.3648041

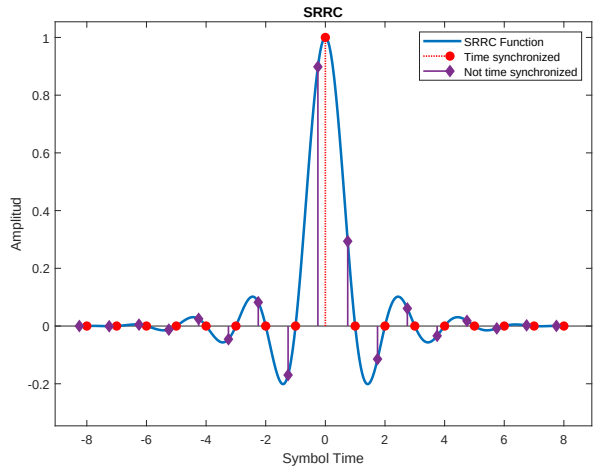

Fig. 3. The blue curve represents the continuous SRRC filter function. In contrast, the red circles indicate the discrete weights used to weight the output of the synchronized symbols, while the purple diamonds represent the weights applied to the non-synchronized symbols.

As such, to analyze the ISI introduced by the time misalignment, a block of more than two symbols must be considered. Suppose that the ISI spreads over K sets of stacked (as in (6)) consecutive symbols $\mathbf{s}_K$, one can re-express (1) and (2) in matrix form as

$$\mathbf{r}_{1K} = ((\mathbf{I}\otimes\mathbf{A}_1)+\mathbf{G}(\mathbf{I}\otimes(\mathbf{H}_2\mathbf{A}_2)))\mathbf{s}_K+\mathbf{z}_K, \quad (9a)$$

$$\mathbf{r}_{2K} = ((\mathbf{I}\otimes\mathbf{A}_2)+\mathbf{G}^T(\mathbf{I}\otimes(\mathbf{H}_1\mathbf{A}_1)))\mathbf{s}_K+\mathbf{z}_K, \quad (9b)$$

wherein, $\mathbf{I}$ be the identity matrix with dimensions $(K\times K)$, $\mathbf{G}$ being a matrix function of the symbol time misalignment between the signals, formed as a block-circulant $(4K\times 4K)$ matrix whose rows are the shifted values of the overall (transmitter and receiver) SRRC function evaluated on the parameter τ_n.

Fig. 3 shows the difference in the ISI contribution of the SRRC filter when the input symbols are time synchronized vs when they are not. For the case of $\tau_n = 0$ (time synchronized symbols), $\mathbf{G}=\mathbf{I}$, however, when $\tau_n \neq 0$ (not time synchronized symbols), $\mathbf{G}\neq\mathbf{I}$.

As in any practical system, the parameters τ_n, α_n, and θ_n used to describe the received signal model must be estimated, hence, the estimated (imperfect) values may differ from the actual (perfect) ones. For the case of time misalignment estimation, we can define the imperfect estimation as:

$$\tilde{\tau}_n = \tau_n + \tau_\epsilon \quad (10)$$

Where τ_ϵ is the error of the estimation. Furthermore, since the matrix $\mathbf{G}$ is formed using the estimated values of the misalignment, the imperfect version of it would be defined as:

$$\tilde{\mathbf{G}}(\tau_n+\tau_\epsilon) = \mathbf{G}+\mathbf{G}_\epsilon \quad (11)$$

Where $\mathbf{G}_\epsilon$ would be an error in the representation of the ISI contribution from the SRRC filter.

On the other hand, the relationship between the perfect and imperfect CSI estimation can be expressed as in [28]:

$$\tilde{h}_i = \sqrt{1-\sigma_h^2}h_i + \sqrt{\sigma_h^2}h_\epsilon \quad (12)$$

Where σ_h^2 is the estimator error variance, and h_ϵ is the error which follows a normal distribution $\mathscr{CN}(0,\sigma_h^2)$.

If we define the effective channel matrices in (9a) and (9b) as the following quantities

$$\mathbf{\Psi}_1 = (\mathbf{I}\otimes\mathbf{A}_1)+\tilde{\mathbf{G}}(\mathbf{I}\otimes(\tilde{\mathbf{H}}_2\mathbf{A}_2)), \quad (13a)$$

$$\mathbf{\Psi}_2 = (\mathbf{I}\otimes\mathbf{A}_2)+\tilde{\mathbf{G}}^T(\mathbf{I}\otimes(\tilde{\mathbf{H}}_1\mathbf{A}_1)), \quad (13b)$$

we can recover the transmitted symbols via pseudo-inverse approximation given by

$$\tilde{\mathbf{s}}_{1K} = \underbrace{\left(\mathbf{\Psi}_1{}^\top\mathbf{\Psi}_1\right)^{-1}\mathbf{\Psi}_1{}^\top}_{\mathbf{\Gamma}_{\text{sol1}}}\mathbf{r}_{1K}, \quad (14a)$$

$$\tilde{\mathbf{s}}_{2K} = \underbrace{\left(\mathbf{\Psi}_2{}^\top\mathbf{\Psi}_2\right)^{-1}\mathbf{\Psi}_2{}^\top}_{\mathbf{\Gamma}_{\text{sol2}}}\mathbf{r}_{2K}. \quad (14b)$$

Herein, $\mathbf{\Gamma}_{\text{sol1}}$ will be called solution matrix 1 and $\mathbf{\Gamma}_{\text{sol2}}$ will be solution matrix 2. For the final approximation of the transmitted symbols, we use the maximum ratio combining of the two branches as

$$\tilde{\mathbf{s}_K} = \frac{|h_1|\tilde{\mathbf{s}_{1K}}+|h_2|\tilde{\mathbf{s}_{2K}}}{|h_1|^2+|h_2|^2}. \quad (15)$$

An analytical expression for the SINR after the combining was developed in our previous work [22] and is given by

$$SINR = 10log_{10}\left(\frac{\sigma_s^2}{\sigma_z^2}\right) - 10log_{10}\left(\frac{\|\mathbf{\Gamma}_{\text{sol}}\boldsymbol{Q}\|_F^2}{2K}\right), \quad (16)$$

where σ_s^2 is the variance of the transmitted symbols, σ_z^2 represents the variance of the filtered noise, $\mathbf{\Gamma}_{\text{sol}} = [\mathbf{\Gamma}_{\text{sol1}};\mathbf{\Gamma}_{\text{sol2}}]$ is the concatenated solution matrices for each branch and $\boldsymbol{Q} = [Q_1;Q_2]$ denotes the matrix for the AWGN at the receiver, filtered by the SRRC and downsample by a factor of 4.

B. Numerical approach

To implement the analytical approach presented above, one must find efficient numerical methods for calculating the solution matrices $\mathbf{\Gamma}_{\text{sol1}}$, $\mathbf{\Gamma}_{\text{sol2}}$ and multiply them by the incoming symbols. While analyzing (14a) and (14b), it becomes evident that, following a classical linear algebra approach, two matrix multiplications and one matrix inversion are required to compute $\mathbf{\Gamma}_{\text{sol1}}$ and $\mathbf{\Gamma}_{\text{sol2}}$. Due to the time-varying nature of the parameters h_1, h_2, and τ_n, both solution matrices must be updated rapidly to track channel variations and adapt to varying conditions without significantly degrading system performance. Although matrix inversion is a common operation in adaptive communication systems, its computational complexity increases rapidly with matrix size. Consequently, considerable research work has been focused on exploiting specific matrix structures to reduce the complexity of inversion algorithms [23].

From (13a) and (13b), it can be noticed that all Kronecker products are performed between an identity matrix $\boldsymbol{I}$ of dimensions $(K \times K)$ and squared matrices of dimensions (4×4), which leads to block-circulant matrices of dimension $(4K \times 4K)$. On the other hand, the structure of the $\mathbf{G}$ matrix is also block-circulant with dimensions $(4K \times 4K)$. Therefore, $\boldsymbol{\Psi}_1$ and $\boldsymbol{\Psi}_2$ are block-circulant matrices composed of K smaller (4×4) real matrices $\varphi_1, \cdots \varphi_K$ in each of the K rows, represented as $\boldsymbol{\Psi}_i$, $i \in \{1,2\}$

$$\boldsymbol{\Psi_i} = \begin{bmatrix} \varphi_1 & \varphi_2 & \cdot & \cdot & \varphi_{K-1} & \varphi_K \\ \varphi_K & \varphi_1 & \cdot & \cdot & \varphi_{K-2} & \varphi_{K-1} \\ \varphi_{K-1} & \varphi_K & \cdot & \cdot & \varphi_{K-3} & \varphi_{K-2} \\ \cdot & \cdot & \cdot & \cdot & \cdot & \cdot \\ \varphi_2 & \varphi_3 & \cdot & \cdot & \varphi_K & \varphi_1 \end{bmatrix}. \tag{17}$$

One advantage of block-circulant matrices is that their inverse can be calculated relatively easily with the help of the Discrete Fourier Transform (DFT). A description of such an approach is proposed in [23], and is based on an extension of the Fourier decomposition of circulant matrices.

If a circulant matrix $\boldsymbol{C}_{N\times N}$ is composed of shifted versions of a column vector $\boldsymbol{c}_{N\times1}$, then such a matrix can be decomposed as

$$\boldsymbol{C} = \boldsymbol{F}^{\boldsymbol{H}} \left(\text{diag}\left(\sqrt{N} \boldsymbol{F} \boldsymbol{c} \right) \right) \boldsymbol{F}, \tag{18}$$

with $\boldsymbol{F}$ represents the Fourier unitary matrix, whose components are $f_{n,k} = \exp\left[\frac{-j2\pi nk}{N}\right]$. Further, the inverse $\boldsymbol{C}^{-1}$ can be given as

$$\begin{aligned} \boldsymbol{C^{-1}} &= \left(\mathbf{F}^H \, \text{diag}\left(\sqrt{N} \mathbf{F} \boldsymbol{c} \right) \mathbf{F} \right)^{-1} \\ &= \mathbf{F}^{-1} \, \text{diag}^{-1}\left(\sqrt{N} \mathbf{F} \boldsymbol{c} \right) \left(\mathbf{F}^H \right)^{-1} \\ &= \mathbf{F}^H \, \text{diag}^{-1}\left(\sqrt{N} \mathbf{F} \boldsymbol{c} \right) \mathbf{F}. \end{aligned} \tag{19}$$

This approach can be naturally extended to compute the pseudo-inverse required for obtaining the solution matrices $\boldsymbol{\Gamma}\text{sol}_\mathbf{1}$ and $\boldsymbol{\Gamma}\text{sol}_\mathbf{2}$, without introducing significant additional complexity. For this purpose, we define the (4×4) complex matrices $\varphi^{(1)}, \ldots, \varphi^{(K)}$, which are related to $\varphi_1, \ldots, \varphi_K$ through the DFT relations as

$$\varphi_k = \sum_{n=1}^{K} \varphi^{(n)} \alpha_n^{k-1}, \quad k = 1, \cdots, K, \tag{20a}$$

$$\varphi^{(n)} = \frac{1}{K} \sum_{k=1}^{K} \varphi_k \left(\alpha_n^* \right)^{k-1}, \quad n = 1, \cdots, K, \tag{20b}$$

with $\alpha_n = \exp\left[j \frac{2\pi}{K} (n-1) \right]$. Now, one can compute $\boldsymbol{\Gamma}_{\text{soli}}, i \in \{1,2\}$ as

$$\boldsymbol{\Gamma}_{\mathbf{soli}} = \begin{bmatrix} \xi_1 & \xi_2 & \cdot & \cdot & \xi_{K-1} & \xi_K \\ \xi_K & \xi_1 & \cdot & \cdot & \xi_{K-2} & \xi_{K-1} \\ \xi_{K-1} & \xi_K & \cdot & \cdot & \xi_{K-3} & \xi_{K-2} \\ \cdot & \cdot & \cdot & \cdot & \cdot & \cdot \\ \xi_2 & \xi_3 & \cdot & \cdot & \xi_K & \xi_1 \end{bmatrix}, \tag{21}$$

$$\text{with } \xi_k = \frac{1}{(K)^2} \sum_{n=1}^{K} \alpha_n^{k-1} \left(\left(\varphi^{(n)} \right)^H \varphi^{(n)} \right)^{-1} \left(\varphi^{(n)} \right)^H. \tag{22}$$

Algorithm 1 Filters coefficients generation using DFT approach.

1: Set $\tau_n \Leftarrow (\tau_{1n} - \tau_{2n})$.
2: Set $\boldsymbol{G} \Leftarrow SRRC(\tau_n)$.
3: Form $\boldsymbol{H}$ using (8).
4: Form $\boldsymbol{\Psi}$ using (13a) or (13b).
5: Set $\varphi^{(n)} \Leftarrow FFT(\varphi_k)$.
6: **for** $n = 1, 2, \ldots, K$ **do**
7: Set $\gamma^{(n)} \Leftarrow \left(\left(\varphi^{(n)} \right)^H \varphi^{(n)} \right)^{-1} \left(\varphi^{(n)} \right)^H$.
8: **end for**
9: Set $\xi_k \Leftarrow IFFT(\gamma^{(n)})$.
10: Update filters coeffs with ξ_k.

Herein, ξ_k is a real matrix of dimension (4×4). Once again, we can leverage the block-circulant structure of the solution matrix when multiplying it by the incoming symbols. This process can be made relatively simple, since multiplying a row vector by a block-circulant matrix (as in (14a) and (14b)) is equivalent to performing a circular convolution between the first row of blocks in the solution matrix, and the row vector. Furthermore, circular convolution can be approximated by linear convolution if one of the sequences is padded with zeros at the beginning and the end as

$$\tilde{\mathbf{s}_{iK}} = \boldsymbol{\xi}_K \circledast \mathbf{r}_{iK} \approx [\mathbf{0} \boldsymbol{\xi}_K \mathbf{0}] * \mathbf{r}_{iK}. \tag{23}$$

It's noteworthy that linear convolution is a well-researched topic and can be easily implemented in the form of an FIR filter.

C. Implementation

To implement the (2×1) combiner at the receiver, a hybrid design approach is adopted, integrating both software and hardware components, as illustrated in Fig. 4. The most time-critical operation, combining the incoming symbols using FIR filter banks, was implemented in hardware (Fig. 5). In contrast, the solution matrix does not require updates at every symbol period; it only needs to adapt quickly enough to track variations in the propagation channel. Therefore, Algorithm 1, which generates the filter coefficients, was implemented in software. This approach also enables the use of floating-point arithmetic during the pseudo-inverse computation, thereby avoiding quantization errors associated with fixed-point representations.

Once the coefficients are generated, the filters are updated with the first four rows of the solution matrix. Each ξ_k block is a real matrix of 4×4, hence the total number of coefficients will be $4 \times 4 \times K$. The output of each filter is downsampled by a factor of 4, and then a selector switches continuously from the output of each downsampler.

IV. EXPERIMENTAL TESTBED

To emulate the scenario in Fig. 1, we used three USRPs from National Instruments, one for the GW, one for the channel emulator, and one for the UT interconnected,

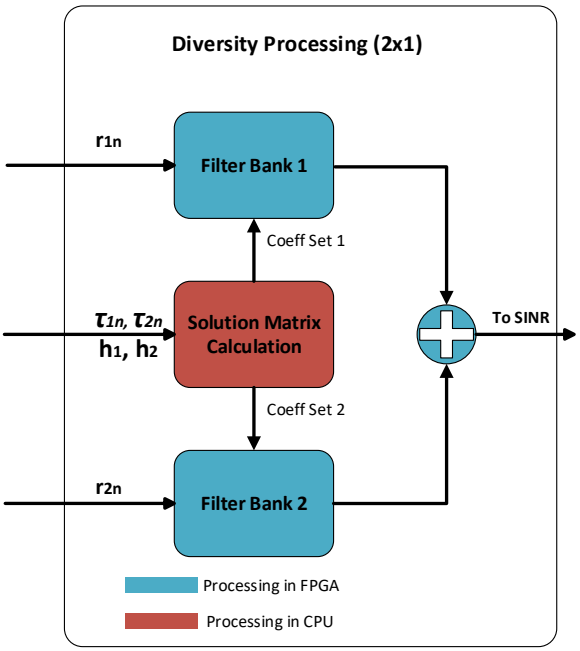

Fig. 4. Internal structure of the 2 × 1 diversity processing block in Fig. 2. The channel coefficients and time misalignment estimation are sent to an embedded processor, which generates the solution matrices. This processor later updates the filter coefficients in the hardware.

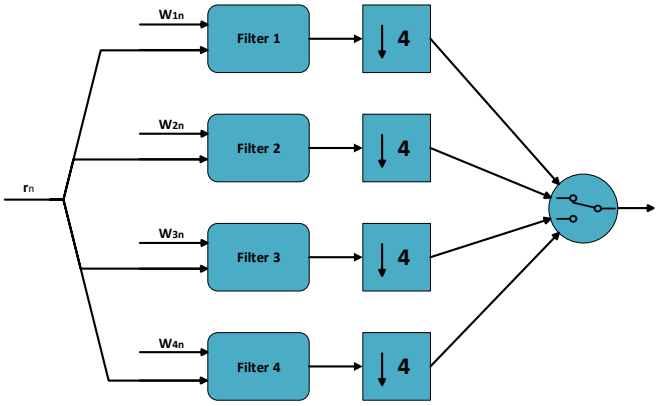

Fig. 5. FIR filter bank used to perform linear convolution between the incoming symbols (is stack representation as in (6)) and the first four rows of the corresponding solution matrix.

as shown in Fig. 6. The GW and channel emulator were implemented on the USRP model 2944R, which features an internal field programmable gate array (FPGA) Kintex-7 410T from Xilinx (AMD). On the other hand, the UT was implemented on a USRP model 2974 owing to the additional presence of an internal Intel Core i7 6822EQ processor, which communicates through PCI Express with the FPGA (same family as in the 2944R), which makes this model ideal for the fast interactions required between the software and hardware parts of the design.

As previously mentioned, we selected the DVB-S2X waveform standard with superframe format two owing to the stringent timing and phase synchronization requirements of the system. The Walsh-Hadamard sequences

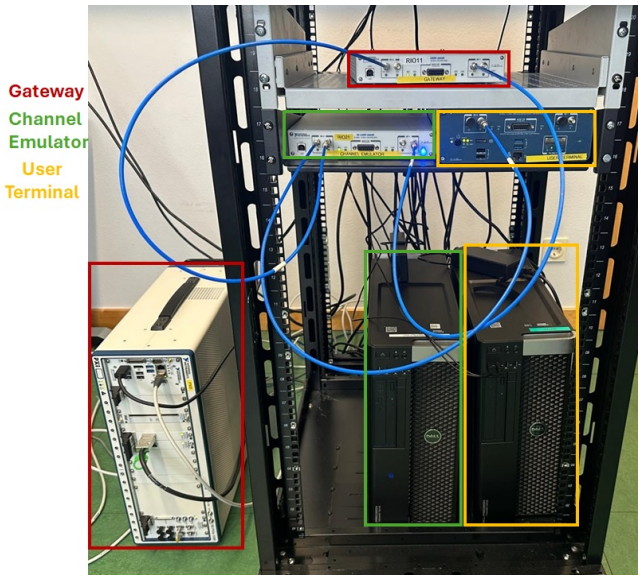

Fig. 6. 2 × 1 Diversity combining Test-Bed. Each USRP is connected to a PC running LabVIEW which is used to initialize and configure the experiments.

used in the Start of Superframe (SOSF) and Pilot (P) fields enable robust synchronization, even under low SNR and high-interference conditions [29].

Fig. 7 illustrates a diagram of the GW in which random data bits are generated, mapped into M-PSK symbols, encoded, and transmitted through the two RF outputs of the 2944R USRP.

An important aspect to consider in the GW design is the impact of the scrambler on the non-synchronized symbols in (9a) and (9b). The ISI introduced by timing misalignment, as the signal passes through the SRRC filter at the UT, affects the scrambled symbols. However, the compensation for this timing misalignment occurs after the symbols are descrambled. As a result, the ISI that is compensated does not match the ISI originally introduced by the SRRC filter (see proof in Appendix A). For this reason, in our experiments, we chose to deactivate the data scrambler while keeping the synchronization sequence scrambler active. This configuration is feasible due to the two-way scrambler mechanism defined in the DVB-S2X standard.

To validate the proposed design, we partially emulated the scenario depicted in Fig. 1 using a satellite link channel emulator, whose block diagram is shown in Fig. 8. This setup enabled us to extend the experimental validation beyond software-based simulations. The emulator introduces controllable impairments, including differential delays [30] and amplitude, phase rotation, and additive noise [31]. The last step in the channel emulator is to add the signals into a single stream and transmit it to the UT. This configuration is illustrated in Fig. 6, where two input lines from the GW feed into the channel emulator, and a single output line connects the emulator

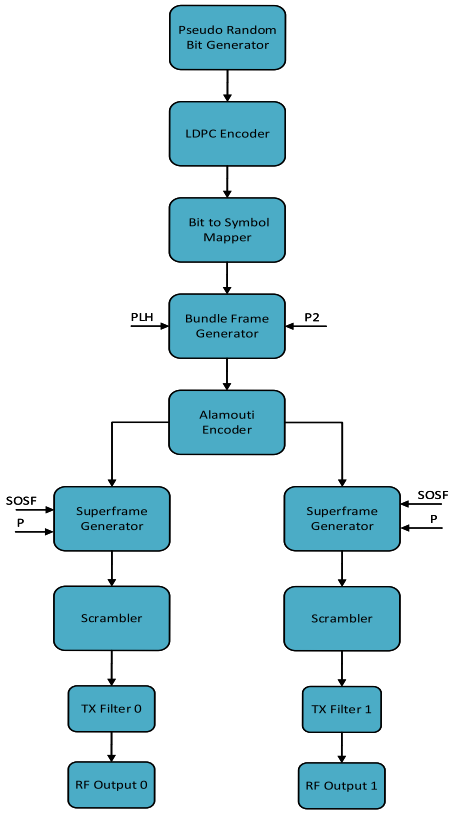

Fig. 7. **In the Gw diagram, the Alamouti encoder is placed after the bundle frame generation but before the superframe generator so that the synchronization sequences (SOSF and P) can be used in the synchronization process needed at the UT before the combining.**

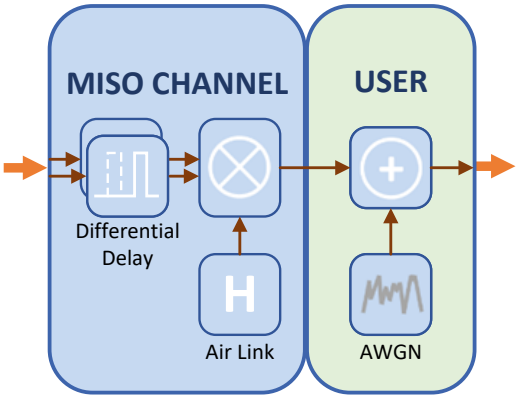

Fig. 8. **Satellite link channel emulator. Differential Delay: Allows for the control of the sample time misalignment between waveforms. Air Link (Channel Matrix): Is used to apply phase rotation and change the amplitude of the signals. AWGN: Introduces Gaussian noise to the link.**

to the UT. A detailed description of the communication link parameters is provided in Table 1.

V. NUMERICAL RESULTS

The evaluation phase was divided into two categories: (i) experiments with constant channel impairments, including time misalignment, phase offset, and power imbalance, and (ii) experiments with time-varying channel impairments. The former were conducted using both software simulations and hardware implementations, while the latter were limited to software-based testing. In all cases, the primary performance metric was the SINR, as it directly reflects the impact of channel distortions such as differential phase rotation, symbol time misalignment, power imbalance, and additive noise, nevertheless the symbol error rate (SER) after the combining process was also analyzed. The numerical results demonstrate that the proposed receiver significantly mitigates SINR degradation caused by symbol time misalignment and enhances the robustness of the communication link against the aforementioned impairments.

TABLE 1. **Communication Link Parameters**

Waveform	DVB-S2X format 2
Transmitted Signals	2
Walsh-Hadamard indices	5 and 13
Modulation Scheme	QPSK
Bandwidth	3.1 MHz
Oversampling Factor	4
SRRC Parameters	filter span=80 symbols, roll-off factor=0.2
SNR of individual signals	Variable
Symbols Time Misalignment	Variable, between -0.5 and 0.5 (-2 to 2 samples)
Uplink carrier frequency (GW to channel emulator)	1.13 GHz
Downlink carrier frequency (channel emulator to UT)	1.376 GHz

When transmitting a signal using Alamouti's scheme with two antennas, an expected SINR gain of 3 dB can be achieved after combining the signals [3]. However, this gain is contingent upon two critical conditions: precise time alignment and equal amplitude of both signals. If a fractional symbol-time misalignment is introduced between the waveforms, the resulting combined SINR undergoes significant degradation, primarily due to ISI induced by the SRRC filter at the UT, as detailed in (1) and (2).

A. SINR gain with constant impairments

Figs. 9, 10, and 11 illustrate the SINR improvements achieved through the methods described in Section III. The blue curve represents the SNR of a single beam (i.e., the signal from an individual satellite), while the remaining four curves depict the SINR of combined signals under both synchronous (zero symbol time misalignment) and asynchronous (non-zero symbol time misalignment) combining scenarios. In the synchronous case, the combined signals exhibit a 3 dB SINR gain relative to the individual beams from each satellite. However, as time misalignment increases, the SINR performance of the classic Alamouti combining receiver (red curve) degrades significantly. Notably, the combined signals most susceptible to time misalignment are those with higher individual SNR, where the

This article has been accepted for publication in IEEE Open Journal of the Communications Society. This is the author's version which has not been fully edited and content may change prior to final publication. Citation information: DOI 10.1109/OJCOMS.2025.3648041

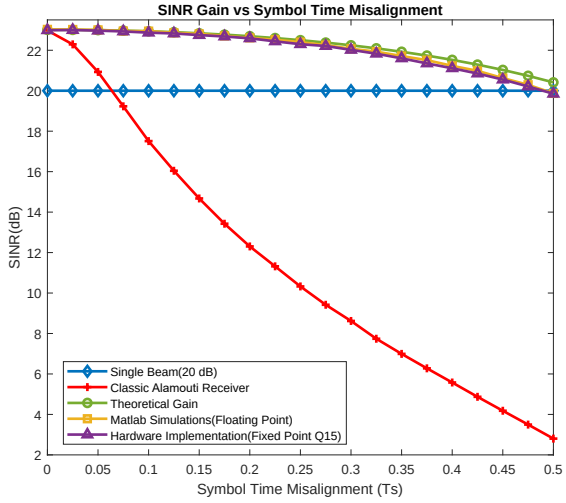

Fig. 9. **SINR in Alamouti's scheme vs symbol time misalignment when combining two signals with 20 dB of SNR each and a differential phase of 2.3 Radians using the proposed methods from section III.**

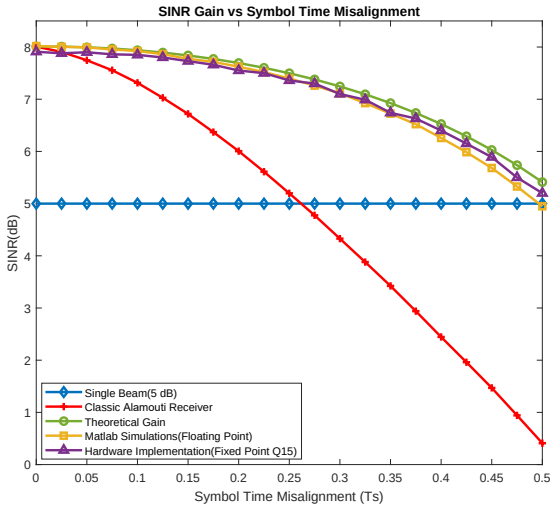

Fig. 11. **SINR in Alamouti's scheme vs symbol time misalignment when combining two signals with 5 dB of SNR each and a differential phase of 1.85 Radians using the proposed methods from section III.**

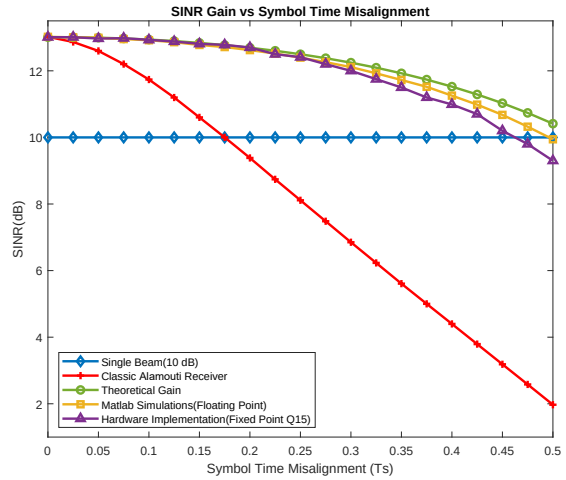

Fig. 10. **SINR in Alamouti's scheme vs symbol time misalignment when combining two signals with 10 dB of SNR each and a differential phase of 0.75 Radians using the proposed methods from section III.**

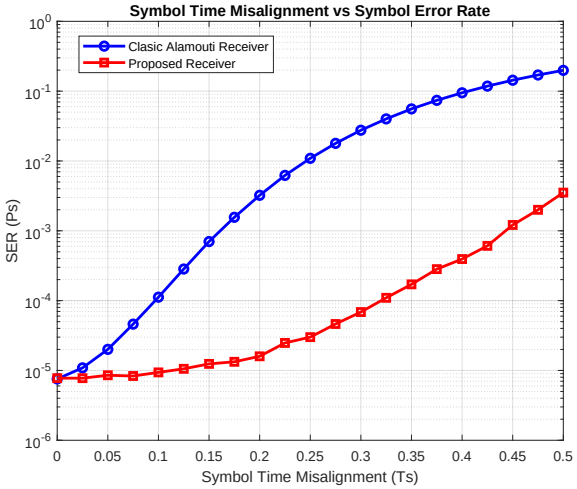

Fig. 12. **Symbol Error Rate performance under symbol time misalignment when combining two signals with individual SNR of 10 dB (combined SINR of 13 dB).**

impact of ISI is more pronounced. In contrast, signals with lower individual SNR exhibit less degradation from ISI, as additive noise becomes the dominant factor affecting signal quality. On the other hand, the proposed combining method demonstrates strong resilience to such degradation. Specifically, the green curve shows the theoretical SINR gain, the yellow curve presents results from MATLAB simulations, and the purple curve reflects measurements obtained from hardware implementation using 16-bit fixed-point arithmetic. Notably, even when the symbol time misalignment reaches 0.5, resulting in a loss of combining gain, the SINR degradation remains limited to approximately 3 dB. Furthermore, the close alignment among theoretical predictions, simulation outcomes, and hardware measurements underscores the robustness and practical viability of the proposed approach. It is worth noting that the differential phase values shown in the figures are those estimated in real time during the hardware experiments.

If we consider the case with the SNR regime of 10 dB for individual signals and analyze the SER (Fig. 12), it becomes obvious how the proposed receiver outperforms the classic Alamouti receiver when time synchronization between the signals is lost.

In most cases, signals transmitted from distributed satellites arrive at the receiver with different amplitudes, a phenomenon known as power imbalance. This effect is primarily caused by variations in propagation path lengths and fading events. In waveform standards such as DVB-

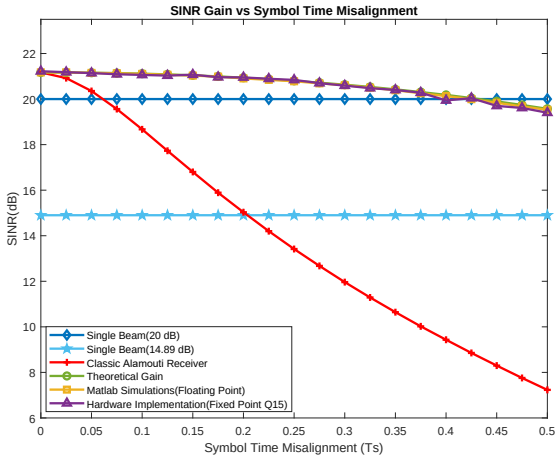

Fig. 13. SINR in Alamouti's scheme vs symbol time misalignment when combining two signals with 5.10 dB of power imbalance. The first signal has an individual SNR of 20 dB, while the second 14.9 dB. In this case, the differential phase is 2.5 Radians.

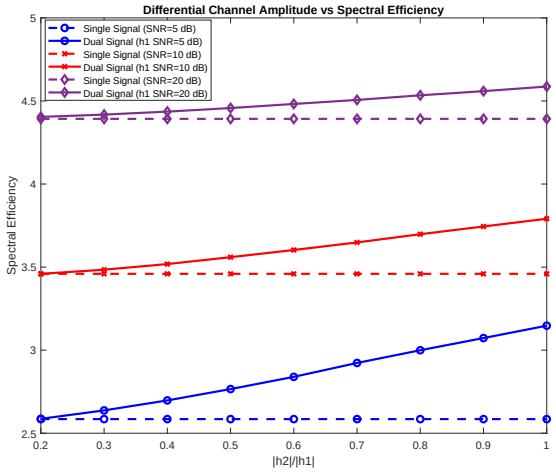

Fig. 14. Spectral efficiency of the proposed system in comparison with the one expected for single signal transmission. For the case of combining individual signals with 5, 10 and 20 dB of indiviidual SNRs.

S2X, adaptive modulation and coding (modcod) schemes are typically employed, thus a degradation in signal SNR often results in a shift to a lower-order modulation and a higher Forward Error Correction (FEC) rate, leading to reduced throughput. Therefore, the capability of providing a semi-stable SINR gain under time-varying channel conditions is a highly desired one. Figs. 13 illustrates the SINR gain achieved when combining two signals with more than 5 dB of power imbalance. It can be noticed that the system consistently maintains a combined SINR that exceeds the higher of the two individual SNRs for most values of symbol time misalignment.

When analyzing the system in terms of spectral efficiency, a combining gain of approximately 3 dB under perfect alignment conditions is expected to enhance performance compared to single-signal transmission. Figure 14 illustrates the spectral efficiency as a function of the ratio between the channels' amplitudes, where the values of $|h_2|$ remain constant as the ones for $|h_1|$ increase from 0.2 to 1 (equal amplitude). When the values of $|h_1|$ are significantly lower than those of $|h_2|$, the spectral efficiency approaches that of a single-channel transmission. However, as the amplitudes of both channels become comparable, the overall spectral efficiency of the system increases, demonstrating the benefit of signal combining.

B. Effect of imperfect parameter estimation

The system performance critically depends on the accurate representation of the effective channel matrices, denoted as $\Psi_{1,2}$. Consequently, it is essential to analyze how estimation errors in symbol time misalignment and differential CSI influence the achievable combining gain. Fig. 15 shows the SINR performance when an error is introduced in the symbol time misalignment estimation with values τ_ϵ= 0%, 1%, 2%, 3% and 4% of the total symbol period.

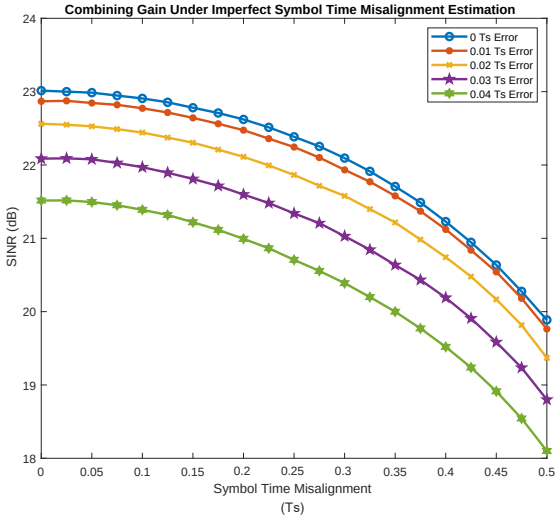

Fig. 15. SINR of combined signals with individual SNR of 20 dB under imperfect symbol time misalignment estimation.

Another critical aspect is the impact of symbol time misalignment on the estimation of CSI in overlapped waveforms. It is well established that perfectly aligned Walsh Hadamard sequences (like the ones used in the pilot fields) exhibit complete orthogonality. However, when this orthogonality degrades due to time misalignment, the variance of the CSI estimator increases accordingly. (Fig. 16).

As it is to be expected, an increase in the variance of the CSI estimation has a negative impact on the resulting SINR after combining. Fig 17 shows the degradation in the combining gain when the variance from Fig. 16 is introduced into the CSI estimation used to generate the solution matrices. Similar results are show in Fig. 18 where

This article has been accepted for publication in IEEE Open Journal of the Communications Society. This is the author's version which has not been fully edited and content may change prior to final publication. Citation information: DOI 10.1109/OJCOMS.2025.3648041

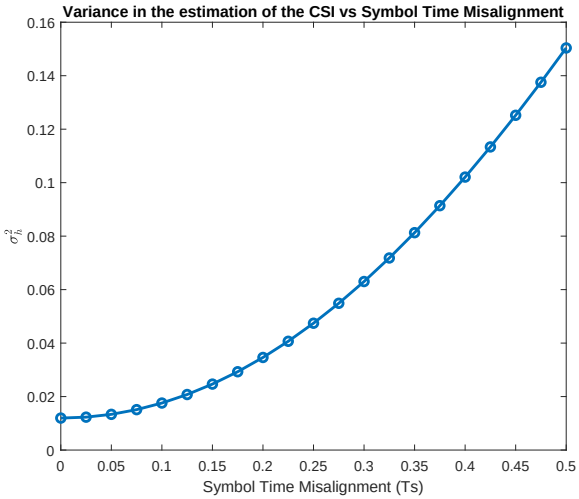

Fig. 16. Variance in the CSI estimation under imperfect pilot alignment.

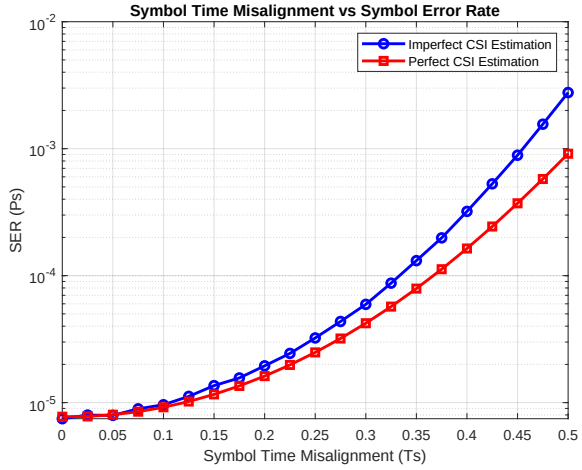

Fig. 18. Symbol Error Rate for performance under imperfect CSI estimation, when combining two signals with individual SNR of 10 dB.

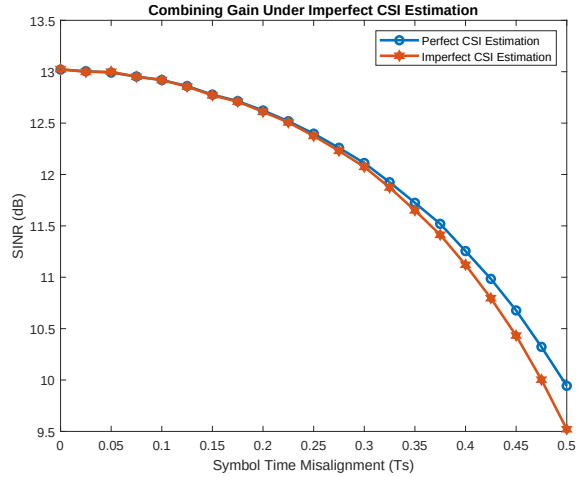

Fig. 17. Effect of variance in the CSI estimation when combining two signals with individual SNR of 10 dB.

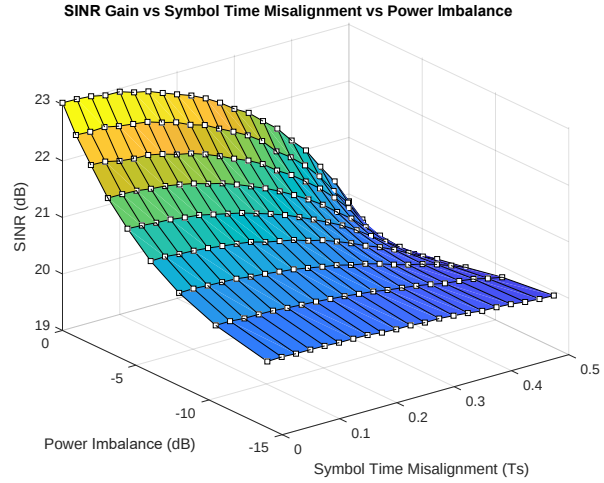

Fig. 19. SINR gain vs symbol time misalignment vs power imbalance, when combining two signals of 20 dB of SNR each and the power of one signal is decreased in steps from 20 dB down to to 6 dB.

an increse in SER can be noticed for an imperfect CSI estimation.

C. SINR gain with time-varying impairments

Differential delay between waveforms is not the only factor that changes when signals are received from distributed satellites. Variations in power imbalance also play a significant role. Moreover, Doppler-induced frequency shifts introduce rapid phase rotations in the symbol constellation, which can further degrade system performance.

Figs. 19 illustrates the variation in SINR gain as a function of symbol time misalignment and power imbalance for the high SNR regime. In this analysis, the SNR of one signal is progressively reduced, introducing a power imbalance of up to 14 dB between the signals, while the misalignment is incrementally increased from 0 to 0.5 symbol time. As observed, the system consistently maintains a quasi-stable SINR, with degradations limited to approximately 3 dB even in the worst-case scenario of 0.5 Ts misalignment. This is possible due to the redundancy provided by the power stability of the signal with the stable (time-invariant) amplitude.

One of the key parameters for effective signal combining using Alamouti's scheme is the differential phase between the incoming symbols. In satellite communication systems, however, this differential phase can exhibit rapid variations when signals originate from different satellites. These fluctuations are primarily caused by frequency shifts resulting from the Doppler effect. Although some compensation methods can be employed [32], a remnant Doppler shift (as commonly known) will always persist.

Fig. 20 illustrates the impact of Doppler shifts up to 500 Hz on the SINR gain. The simulations are conducted under the system configuration specified in Table 1, with

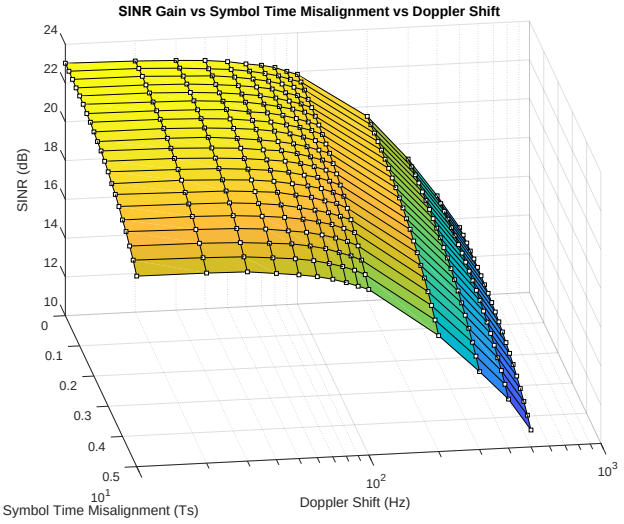

Fig. 20. SINR gain vs symbol time misalignment vs Doppler shift, when combining two signals of 20 dB of SNR each.

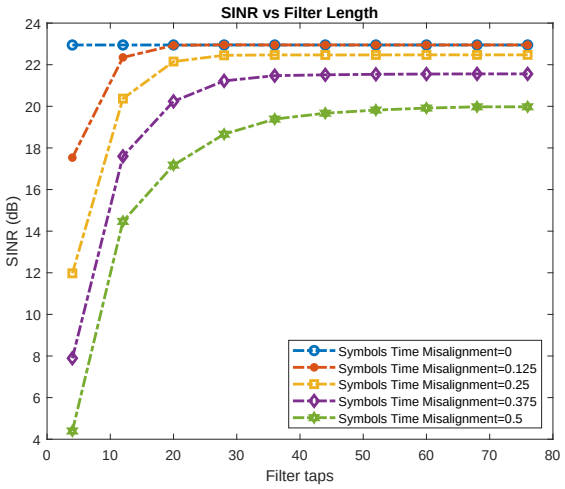

Fig. 21. SINR gain vs filter length when combining two signals with 20 dB of SNR each.

the differential phase measurement updated every 956 symbols, corresponding to the pilot spacing in the DVB-S2X Format 2 standard. As the Doppler shift increases, the SINR gain decreases, reflecting the growing difficulty of the synchronization system in accurately tracking the differential phase between signals.

D. Filter length impact in SINR and computational complexity

One critical aspect of our design is the analysis of the combining filters length. Filters with too few taps fail to adequately compensate for the ISI introduced by the SRRC filter, while excessively long filters increase computational complexity without significant performance gains. An upper bound for the filter length can be defined based on the symbol span of the SRRC filter, which in our case is 80 symbols. To determine a suitable lower bound, we conducted experiments analyzing the SINR gain as a function of the number of taps in the filter bank, under varying conditions of symbol time misalignment and individual SNR.

For the scenario with individual signal SNRs of 20 dB (Fig. 21), it can be observed that lower time misalignments between signals require fewer filter taps to effectively compensate for ISI. Moreover, beyond 60 taps, the SINR gain saturates, even in the worst-case misalignment of 0.5 Ts.

Since the receiver is fully implemented in an embedded system, computational resources are limited. Therefore, each arithmetic operation must be carefully examined to ensure efficiency. Given the division between software and hardware components, it is appropriate to conduct separate analyses: one for the floating-point operations executed in software, and another for the fixed-point operations carried out in hardware.

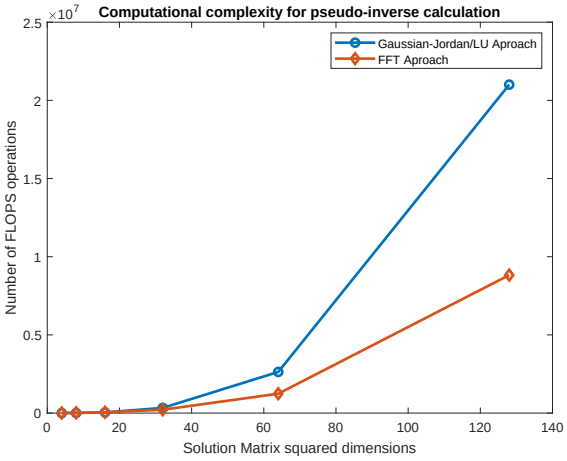

Fig. 22. Computational complexity using classical matrix inversion methods vs using our proposed method.

The proposed Algorithm 1 introduces considerable computational complexity. It involves multiple matrix multiplications, both real and complex, with a complexity of $\mathcal{O}(N^3)$, as well as K 4 × 4 complex matrix inversion using either Lower-Upper decomposition or Gauss-Jordan elimination, which also has a complexity of $\mathcal{O}(N^3)$. Additionally, the algorithm performs several Fast Fourier Transform (FFT) computations using the radix-2 algorithm, requiring $\mathcal{O}(\frac{K}{2} log_2(K))$ complex multiplications and $\mathcal{O}(K log_2(K))$ complex additions [33].

Table 2 presents a comprehensive breakdown of the computational complexity involved in calculating the filter coefficients. All complex operations are represented by their equivalent number of real floating-point operations to provide a uniform and precise comparison.

Fig. 22 compares the overall computational complexity of calculating the pseudo inverse in (14a) and (14b), using the proposed Algorithm 1, against conventional matrix

TABLE 2. Floating Point Operations in Algorithm 1 (for an individual Rx chain)

Operation	Description	Complexity (Real Flops)
Computing τ_n	One real substraction	$\mathcal{O}(1)$
Computing $\boldsymbol{G}$	Pre-computed values	-
Form $\boldsymbol{H}$ using (Eq. 8)	Read values from FPGA	-
Form $\boldsymbol{\Psi_{1,2}}$ using (13a) and (13b)	One 4×4 real matrix multiplication, One $N\times N$ real matrix multiplication and one $N\times N$ real matrix addition	$\mathcal{O}(4^3)+\mathcal{O}(N^3)+\mathcal{O}(N^2)$
Compute FFT	Perform 16 FFT of K samples each (where φ_K is composed by K (4×4) matrices)	$16[\mathcal{O}(4(\frac{K}{2})log_2(K))+\mathcal{O}(2(Klog_2(K)+(\frac{K}{2})log_2(K))]$
Compute Pseudo-Inverse of K 4×4 complex matrices	Each complex pseudo inverse requires 2 (4×4) complex matrix multiplication and one 4×4 complex matrix inversion	$\mathcal{O}(2(480))+\mathcal{O}(856)$
Compute IFFT	Perform 16 IFFT of K samples each (where $\gamma^{(n)}$ is composed by K (4×4) matrices)	$16[\mathcal{O}(4(\frac{K}{2})log_2(K))+\mathcal{O}(2(Klog_2(K)+(\frac{K}{2})log_2(K))]$

inversion techniques such as Lower-Upper decomposition and Gauss-Jordan elimination. All matrix sizes are powers of two, in accordance with the radix-2 FFT algorithm requirements. The results indicate that for smaller matrices, the computational complexities are comparable. However, as the matrix size increases, the proposed method demonstrates a notable efficiency gain, requiring less than half the number of floating-point operations for a 64×64 matrix and nearly 2.7 times fewer operations for a 128×128 matrix.

In contrast, hardware complexity analysis is more straightforward. According to digital filter theory, the number of multiplications in an N-tap FIR filter scales with $\mathcal{O}(N)$, and the number of additions scales with $\mathcal{O}(N-1)$ [34]. Fig. 23 illustrates the total number of fixed-point operations per symbol accounting for both filter banks required to merge the two data streams as a function of the filter length.

VI. CONCLUSION

In conclusion, this work introduces a novel receiver architecture tailored for distributed STBC satellite communication scenarios, addressing the critical challenge of symbol-level time misalignment. The proposed system, implemented and validated in both software and hardware environments, leverages adaptive and computationally efficient algorithms to enhance STBC-based combining schemes. By integrating time misalignment information into the combining process, the receiver achieves significant performance gains over conventional approaches, particularly under imperfect signal alignment. The robustness of the system was further demonstrated under typical satellite impairments such as power imbalance and Doppler shift, with consistent SINR and SER performance. A detailed computational complexity analysis was conducted, including the development of an efficient pseudo-inverse computation algorithm for software implementation. Future work will focus on over-the-air validation using real satellite links and the exploration of alternative waveform standards, such as orthogonal frequency-division multiplexing (OFDM) in 5G NR.

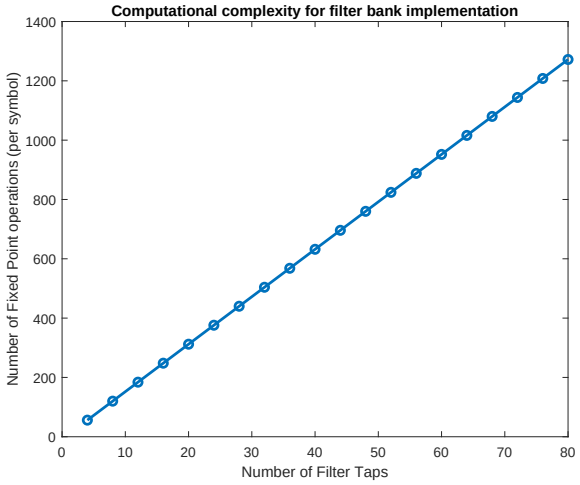

Fig. 23. Computational complexity of the two filter banks used in the combining process.

APPENDIX

A. SCRAMBLER EFFECT ON THE INTER-SYMBOL INTERFERENCE

Suppose we want to transmit a vector of complex symbols $\boldsymbol{x}\in\mathbb{C}$. On the GW side, the symbols are first encoded by a generic encoding matrix $\mathbf{E}$ and then scrambled by a scrambling vector $\boldsymbol{s}$, before going through the transmission filter. On the UT side the received symbols can be expressed as

$$\mathbf{r}=\text{diag}(\boldsymbol{d})\boldsymbol{G}h\,\text{diag}(\boldsymbol{s})\boldsymbol{E}\boldsymbol{x}, \tag{24}$$

where h is a scalar representing the channel CSI that remains constant for the duration of the symbol's transmission, $\boldsymbol{G}$ is the ISI introduced by the SRRC filter due to improper time synchronization, and $\boldsymbol{d}$ is the descrambler sequence applied to the incoming symbols, and has the property $\text{diag}(\boldsymbol{d})\,\text{diag}(\boldsymbol{s})=I$. If we wish to recover the transmitted symbols using the approach proposed in (14a) and (14b) based on the estimation of h and $\boldsymbol{G}$, we can write

$$\begin{aligned}\tilde{\mathbf{x}}=&\Big[\big((\boldsymbol{G}h\boldsymbol{E})^H(\boldsymbol{G}h\boldsymbol{E})\big)^{-1}(\boldsymbol{G}h\boldsymbol{E})^H\Big]\\&\times\Big[\text{diag}(\boldsymbol{d})\boldsymbol{G}\big(\text{diag}(\boldsymbol{s})h\boldsymbol{E}\boldsymbol{x}\big)\Big].\end{aligned} \tag{25}$$

if $\boldsymbol{G} = \boldsymbol{I}$ then (25) transform into:

$$\tilde{\mathbf{x}} = \left[\left((h\boldsymbol{E})^H (h\boldsymbol{E}) \right)^{-1} (h\boldsymbol{E})^H \right] h\boldsymbol{E}\boldsymbol{x}. \tag{26}$$

Then the transmitted symbols can be recovered appropriately, otherwise if a scrambler sequence is used while the signal is affected by improper time synchronization (like the overlapped signals in (9a) and (9b)), the ISI distortion compensated is not the same as the one introduced by the SRRC filter.

REFERENCES

[1] "IRIS: the new EU Secure Satellite Constellation." [Online]. Available: https://defence-industry-space.ec.europa.eu/eu-space/iris2-secure-connectivity_en

[2] A. Modenini, A. Ugolini, A. Piemontese, and G. Colavolpe, "On the use of multiple satellites to improve the spectral efficiency of broadcast transmissions," *IEEE Transactions on Broadcasting*, vol. 61, no. 4, pp. 590–602, Dec. 2015.

[3] S. Alamouti, "A simple transmit diversity technique for wireless communications," *IEEE Journal on Selected Areas in Communications*, vol. 16, no. 8, pp. 1451–1458, 1998.

[4] D. Gesbert, M. Shafi, D. shan Shiu, P. Smith, and A. Naguib, "From theory to practice: an overview of MIMO space-time coded wireless systems," *IEEE Journal on Selected Areas in Communications*, vol. 21, no. 3, pp. 281–302, Apr. 2003.

[5] A. Roy and R. Roy, "Reliability benefit of network coding and cooperative communication," *Physical Communication*, vol. 29, pp. 217–229, 2018.

[6] M. Sellathurai, P. Guinand, and J. Lodge, "Space-time coding in mobile satellite communications using dual-polarized channels," *IEEE Transactions on Vehicular Technology*, vol. 55, no. 1, pp. 188–199, Jan. 2006.

[7] Y. Dhungana, N. Rajatheva, and C. Tellambura, "Dual hop MIMO OSTBC for LMS communication," *IEEE Wireless Communications Letters*, vol. 1, no. 2, pp. 105–108, Apr. 2012.

[8] R.-Y. Wei, K.-H. Lin, and J.-R. Jhang, "High-diversity bandwidth-efficient space-time block coded differential spatial modulation," *IEEE Open Journal of the Communications Society*, vol. 5, pp. 3331–3339, 2024.

[9] M. R. Cribbs, R. A. Romero, and T. T. Ha, "Physical layer security for multiple-input multiple-output systems by alternating orthogonal space-time block codes," *IEEE Open Journal of the Communications Society*, vol. 1, pp. 1503–1523, 2020.

[10] A. Maaref and S. Aissa, "Capacity of space-time block codes in mimo rayleigh fading channels with adaptive transmission and estimation errors," *IEEE Transactions on Wireless Communications*, vol. 4, no. 5, pp. 2568–2578, 2005.

[11] V. Tarokh, H. Jafarkhani, and A. Calderbank, "Space-time block codes from orthogonal designs," *IEEE Transactions on Information Theory*, vol. 45, no. 5, pp. 1456–1467, Jul. 1999.

[12] O. Kodheli, E. Lagunas, N. Maturo, S. K. Sharma, B. Shankar, J. F. M. Montoya, J. C. M. Duncan, D. Spano, S. Chatzinotas, S. Kisseleff, J. Querol, L. Lei, T. X. Vu, and G. Goussetis, "Satellite communications in the new space era: A survey and future challenges," *IEEE Communications Surveys & Tutorials*, vol. 23, no. 1, pp. 70–109, Firstquarter 2021.

[13] R. Mudumbai, D. R. Brown Iii, U. Madhow, and H. V. Poor, "Distributed transmit beamforming: challenges and recent progress," *IEEE Communications Magazine*, vol. 47, no. 2, pp. 102–110, Feb. 2009.

[14] M. A. Vazquez, A. Perez-Neira, D. Christopoulos, S. Chatzinotas, B. Ottersten, P.-D. Arapoglou, A. Ginesi, and G. Taricco, "Precoding in multibeam satellite communications: Present and future challenges," *IEEE Wireless Communications*, vol. 23, no. 6, pp. 88–95, Dec. 2016.

[15] M. Bazdresch and M. Al-Hamiri, "Symbol synchronization of the alamouti space-time block code with the gardner algorithm," in *2017 8th IEEE Annual Information Technology, Electronics and Mobile Communication Conference (IEMCON)*, 2017, pp. 635–639.

[16] V. M. Kapinas, P. Horvath, G. K. Karagiannidis, and I. Frigyes, "Time synchronization issues for quasi-orthogonal space-time block codes," in *2007 International Workshop on Satellite and Space Communications*, 2007, pp. 66–70.

[17] P. Dmochowski and P. McLane, "Timing synchronization for real-valued orthogonal space-time block codes," in *23rd Biennial Symposium on Communications, 2006*, 2006, pp. 177–181.

[18] M.-T. O. E. Astal and J. C. Olivier, "Distributed closed-loop extended orthogonal stbc: Improved performance in imperfect synchronization," in *2013 IEEE 24th Annual International Symposium on Personal, Indoor, and Mobile Radio Communications (PIMRC)*, 2013, pp. 1941–1945.

[19] F.-C. Zheng, A. G. Burr, and S. Olafsson, "Near-optimum detection for distributed space-time block coding under imperfect synchronization," *IEEE Transactions on Communications*, vol. 56, no. 11, pp. 1795–1799, 2008.

[20] Y. Liu, W. Zhang, and P. C. Ching, "Time-reversal space-time codes in asynchronous two-way double-antenna relay networks," in *2015 IEEE International Conference on Acoustics, Speech and Signal Processing (ICASSP)*, 2015, pp. 3118–3122.

[21] C. L. M. Rojas, R. Palisetty, J. Krivochiza, J. L. G. Rios, L. M. Marrero, W. A. Martins, J. C. M. Duncan, and S. Chatzinotas, "Time-misalignment estimation in overlapped dvb-s2x waveforms," in *2024 IEEE Wireless Communications and Networking Conference (WCNC)*, 2024, pp. 1–6.

[22] V. Singh, G. Eappen, W. A. Martins, R. Palisetty, C. L. M. Rojas, J. L. Gonzalez-Rios, J. A. VÃąsquez-Peralvo, J. Krivochiza, J. C. Merlano-Duncan, L. G. Socarras, S. Chatzinotas, and B. Ottersten, "Diversity combining scheme for time-varying STBC NGSO multi-satellite systems," *IEEE Communications Letters*, vol. 28, no. 4, pp. 882–886, Apr. 2024.

[23] R. Vescovo, "Inversion of block-circulant matrices and circular array approach," *IEEE Transactions on Antennas and Propagation*, vol. 45, no. 10, pp. 1565–1567, 1997.

[24] C. A. Corral, "Inversion of matrices with prescribed structured inverses," in *2002 IEEE International Conference on Acoustics, Speech, and Signal Processing*, vol. 2, 2002, pp. II–1501–II–1504.

[25] "A parallel algorithm for the inversion of matrices with simultaneously diagonalizable blocks," *Computers & Mathematics with Applications*, vol. 174, pp. 340–351, 2024.

[26] J. A. Vasquez-Peralvo, J. C. M. Duncan, R. Palisetty, V. Singh, G. Eappen, and J. L. Gonzalez-Rios, "Wide-Beamwidth Circular Polarized Antenna for Diversity Combining Applications," in *2022 IEEE Globecom Workshops (GC Wkshps)*, 2022, Conference Proceedings, pp. 1395–1399.

[27] C. Yuen, Y. L. Guan, and T. T. Tjhung, *Quasi-Orthogonal Space-Time Block Code*. PUBLISHED BY IMPERIAL COLLEGE PRESS AND DISTRIBUTED BY WORLD SCIENTIFIC PUBLISHING CO., 2007. [Online]. Available: https://www.worldscientific.com/doi/abs/10.1142/p524

[28] X. Chen and C. Yuen, "On interference alignment with imperfect csi: Characterizations of outage probability, ergodic rate and ser," *IEEE Transactions on Vehicular Technology*, vol. 65, no. 1, pp. 47–58, 2016.

[29] E. Casini, R. D. Gaudenzi, and A. Ginesi, "Dvb-s2 modem algorithms design and performance over typical satellite channels," *International Journal of Satellite Communications and Networking*, vol. 22, no. 3, pp. 281–318, 2004. [Online]. Available: https://onlinelibrary.wiley.com/doi/abs/10.1002/sat.791

[30] J. L. Gonzalez-Rios, E. Lagunas, H. Al-Hraishawi, L. M. Garces Socarras, and S. Chatzinotas, "In-Lab Carrier Aggregation Testbed for Satellite Communication Systems," in *30th Ka and Broadband Space Communications Conference*, 2025.

[31] G. Eappen, J. L. Gonzalez, V. Singh, R. Palisetty, A. Haqiqtnejad, L. M. Marrero, J. Krivochiza, J. Querol, N. Maturo, J. C. M. Duncan, E. Lagunas, S. Andrenacci, and S. Chatzinotas, "Optimal Linear Precoding Under Realistic Satellite Communications Scenarios," *IEEE Open Journal of Vehicular Technology*, vol. 6, pp. 81–91, 2025.

[32] J. L. Gonzalez-Rios, L. Martinez-Marrero, E. Lagunas, J. Krivochiza, L. M. Garces-Socarras, R. Palisetty, J. M. Duncan, and S. Chatzinotas, "Doppler Shift in Precoded Cooperative Multi-Gateway Satellite Systems: Effects and Mitigation," in *2024 IEEE Wireless Communications and Networking Conference (WCNC)*, 2024, Conference Proceedings, pp. 1–6.

[33] W. H. Press, S. A. Teukolsky, W. T. Vetterling, and B. P. Flannery, *Numerical Recipes in C*. Cambridge: Cambridge University Press, 1992, iSBN 0–521–43108–5.

[34] J. G. Proakis and D. K. Manolakis, *Digital Signal Processing (4th Edition)*. USA: Prentice-Hall, Inc., 2006.